Giant phonon-skyrmion coupling in ferromagnet/heavy metal heterostructures

Egor Savostin[1,3,*] and Vitaliy Lomakin[2,3,1,†]

[1]*Program in Materials Science and Engineering, University of California, San Diego, La Jolla, California 92093, USA*
[2]*Department of Electrical and Computer Engineering, University of California, San Diego, La Jolla, California 92093, USA*
[3]*Center for Memory and Recording Research, University of California, San Diego, La Jolla, California 92093, USA*

The strong impact of the strain-induced Dzyaloshinskii-Moriya interaction (SIDMI) on the magnetization dynamics of skyrmions in nanomagnetic structures is demonstrated. The effects of SIDMI are characterized by skyrmion equations (SEs) of motion and magnetoelastic (ME) equations. The study is performed on a model system of MgO/CoFe/Pt stacked on a piezoelectric substrate. The results demonstrate a major nonlinear amplification in both the first- and higher-harmonic magnitudes of the skyrmion breathing mode due to SIDMI. Remarkably, this enhancement can trigger a skyrmion collapse, enabling its deletion with ultraweak strain-induced excitations. The SIDMI effect is shown to be much more significant than the conventional ME effect. These findings open different avenues for the efficient manipulation of nanomagnetic structures through strain.

I. INTRODUCTION

Spintronics and straintronics play crucial roles in achieving low-energy consumption [1–3], high-density data storage [4], wave computing [5], neuromorphic computing [6], and related applications in emerging electronics platforms. These platforms demand a comprehensive understanding of the nonlinear dynamics of spatially inhomogeneous magnetization states.

Ferromagnetic (FM) materials epitaxially grown in heterostructures experience proximity effects at their interfaces, leading to changes in the free energy. In FM/heavy metal (HM) structures, strong spin-orbit coupling can induce a Dzyaloshinskii-Moriya (DM) antisymmetric exchange interaction [7,8], stabilizing helical magnetic orders. An interfacial DM interaction (DMI) in FM/HM bilayers is typically stronger than that in bulk chiral ferromagnets [9,10]. The interplay between exchange interactions, DMI, surface anisotropy, magnetocrystalline anisotropy, dipole-dipole interactions, and magnetoelastic (ME) interactions can give rise to nontrivial topological magnetic orders, such as skyrmions. Skyrmions can be driven by a dynamic field resulting in a breathing mode (BM) [11,12]. The skyrmion phase may be stabilized with tensile strains in the chiral-lattice insulator Cu_2OSeO_3 with a cubic crystal structure [13]. Ferroelectric/ferromagnetic hybrid wires were shown to serve for skyrmion creation and transport [14]. It was shown [15] that skyrmion motion may be induced by voltage-controlled in-plane strain gradients. The creation and deletion of a skyrmion with strains of 0.1%–1% was demonstrated [16]. The breathing modes of skyrmion crystals were shown to be induced by ac electric fields in Cu_2OSeO_3 [17]. A recent experimental study [18] showed that uniaxial strains may lead to the anisotropy of DMI and significantly affect the

equilibrium magnetization states. Reference [19] explained that the variability in the DMI coefficient is primarily associated with strain-induced alterations in the interatomic distances on the FM/HM interface. This opens ways of manipulating magnetization in nanomagnetic structures by strain and phonon coupling.

Here, we show that strain-induced DMI (SIDMI) leads to giant nonlinear effects on the skyrmion dynamics, including enhanced higher-harmonic generation and skyrmion collapse by ultralow strains of only 0.01% in the 1.8–2 GHz frequency range. We derive a SIDMI form based on all strain components and show that all of them play an important role. We use skyrmion equations (SEs) of motion and a coupled system of ME equations to characterize the dynamic effects. We consider an MgO/CoFe/Pt trilayer epitaxially grown on a piezoelectric substrate [Fig. 1(a)] with a bcc lattice. Virtually any realistic piezoelectric substrate can be used for experimental implementations since only weak strains are required. As an example, one may use $Pb(Nb_{2/3}Zn_{1/3})O_3$-$PbTiO_3$ (PZN-PT) [20]. The piezoelectric substrate generates GHz elastic longitudinal waves $\epsilon_{zz}(t)$ that propagate to the trilayer and generate the dynamics of skyrmions. We consider all boundaries of the trilayer to be elastically open, allowing all faces of the nanoheterostructure to absorb elastic excitations, thus eliminating possible elastic resonances and focusing on the strong SIDMI effects on the skyrmion dynamics. The initial stabilization of the skyrmion is performed by applying a weak magnetic field of $H_z = 10^5$ A/m.

II. STRAIN-DRIVEN SKYRMION DYNAMICS

A. Strain-induced DMI

To describe the SIDMI, we formulate the quantum spin energy operator, i.e., Hamiltonian,

$$\hat{H}_D = \sum_{\langle i,j \rangle} \boldsymbol{D}_{ij}[\boldsymbol{m}_i \times \boldsymbol{m}_j]. \tag{1}$$

*Contact author: esavostin@ucsd.edu
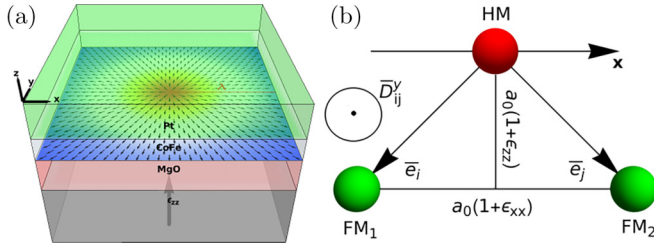†Contact author: vlomakin@ucsd.edu

FIG. 1. (a) A single skyrmion formed in a CoFe layer in the MgO/CoFe/Pt structure grown on a piezoelectric substrate. (b) Atomic triangle of indirect exchange on the CoFe/Pt interface. Crystallographic axes coincide with the Cartesian coordinates.

This Hamiltonian describes the indirect exchange between neighboring spins mediated by an impurity with a large spin-orbit coupling (SOC). The spatially dependent vector $\boldsymbol{D}_{ij}$ between two spins $\boldsymbol{m}_i$ and $\boldsymbol{m}_j$ can be decomposed into scalar and vector components [21] as the product $\boldsymbol{D}_{ij} = V\boldsymbol{R}_{ij} = \boldsymbol{x}D_{ij}^x + \boldsymbol{y}D_{ij}^y + \boldsymbol{z}D_{ij}^z$, where V is a constant and

$$
\begin{aligned}
\boldsymbol{R}_{ij} = \sin[k_F(R_i + R_j + R_{ij}) + \pi Z_d/10] \\
\times \boldsymbol{e}_i \cdot \boldsymbol{e}_j[\boldsymbol{e}_i \times \boldsymbol{e}_j]/(R_i R_j R_{ij})
\end{aligned}
\tag{2}
$$

represents the vectors connecting the SOC center and FM atoms on the interface, R_i is the length between the SOC center and FM atoms, R_{ij} is the distance between the ferromagnetic atoms, k_f is the wave vector on the Fermi surface, and Z_d is the number of d electrons. The SIDMI components can be derived from the geometry of the bcc lattice, which defines the vector product of the directional cosines lying in the x-z plane.

Using the four-neighbor model and symmetry principles, one can show that the DMI vector $D_{ij}^z = 0$ for a perfectly matched FM/HM epitaxial interface [22]. After summing up the contributions of the nearest neighbors we can derive a macroscopic relation of SIDMI:

$$
\begin{aligned}
W_{\text{DMI}}(\epsilon) = D_x(\epsilon_{yy}, \epsilon_{zz})(m_x \partial m_z/\partial x - m_z \partial m_x/\partial x) \\
+ D_y(\epsilon_{xx}, \epsilon_{zz})(m_y \partial m_z/\partial y - m_z \partial m_y/\partial y).
\end{aligned}
\tag{3}
$$

Here, $D_i(\epsilon) = D_0 + \eta_{ij}\epsilon_{jj} + \eta_{iz}\epsilon_{zz}$ represents the strain-dependent anisotropic components of the DMI vector and $\eta_{ij} = \partial D_i/\partial \epsilon_{jj}$ is introduced as a DMI strain sensitivity tensor. The tensor components can be derived by expressing the vector product $\boldsymbol{e}_i\boldsymbol{e}_j[\boldsymbol{e}_i \times \boldsymbol{e}_j]$ defining the orientation of $\boldsymbol{D}_{ij}$ and $R_{ij} = a_0(1 + \epsilon_{mm})$ via in-plain strain components ϵ_{ii} and the out-of-plane component ϵ_{zz}, with a_0 the lattice constant [Fig. 1(b)]. Vector $\boldsymbol{D}_{ij}$ points normal to the plane of an atomic triangle FM$_1$-HM-FM$_2$. For example, an in-plane strain component ϵ_{xx} only alters the distance between the atoms in the x direction in the triangle, defining D_y, which is normal to the x-z plane. Realistic values of η_{ij} typically fall within the range of hundreds of mJ/m^2 [18]. Particularly, we use $\eta_{xz} = \eta_{yz} = \eta_{iz} = 0.5$ J/m^2 and $\eta_{xy} = \eta_{yx} = 0.35$ J/m^2 in the following results.

The elastically induced skyrmion dynamics can be described by the Landau-Lifshitz-Gilbert (LLG) equation $\boldsymbol{m}$,

$$
\frac{\partial \boldsymbol{m}}{\partial t} = -\frac{\gamma \mu_0}{1 + \alpha^2}([\boldsymbol{H}_{\text{eff}} \times \boldsymbol{m}] + \alpha[\boldsymbol{m} \times [\boldsymbol{m} \times \boldsymbol{H}_{\text{eff}}]]).
\tag{4}
$$

The total effective field $\boldsymbol{H}_{\text{eff}} = -(\mu_0 M_s)^{-1}\partial W/\partial \boldsymbol{m}$ acting on the magnetization is a sum of contributions resulting from the exchange coupling W_{ex} that includes a second-order expansion term, DMI $W_{\text{DMI}}(\epsilon)$, bulklike magnetocrystalline anisotropy W_{an}, perpendicular anisotropy W_{pa}, Zeeman energy W_Z, dipole-dipole interactions W_{dm}, and the magnetoelastic energy $W_{\text{me}}(\epsilon)$ given by [23]

$$
\begin{aligned}
W_{\text{me}} = B_1\big[\big(m_x^2 - \tfrac{1}{3}\big)\epsilon_{xx} + \big(m_y^2 - \tfrac{1}{3}\big)\epsilon_{yy} + \big(m_z^2 - \tfrac{1}{3}\big)\epsilon_{zz}\big] \\
+ B_2(m_x m_y \epsilon_{xy} + m_y m_z \epsilon_{yz} + m_z m_x \epsilon_{zx}).
\end{aligned}
\tag{5}
$$

The LLG equation can be solved directly and it can also include the ME coupling involving elastodynamics equations.

B. Skyrmion dynamics via a mean-field model

To obtain a quantitative understanding of the changes occurring in BM due to SIDMI we first develop a mean-field skyrmion model, in which we exclude W_{dm} and shear stresses. The Lagrangian that establishes a canonical conjugate relationship between the generalized momentum and the generalized coordinate for the undamped LLG (4) with $\alpha = 0$ is given by [12]

$$
\mathcal{L} = \frac{M_s}{\gamma} \int_0^\lambda \int_0^{2\pi} \dot{\Phi}(\cos\Theta + 1)r\,dr\,d\phi - E,
\tag{6}
$$

where Φ, Θ are spin projections in a spherical coordinate system. The magnetization precesses around its equilibrium given for the topological charge $Q = 1$ in the polar coordinates $x = r\cos\phi$, $y = r\sin\phi$, $m_x = f(r,\lambda)\cos(\phi + \beta)$, $m_y = f(r,\lambda)\sin(\phi + \beta)$, $m_z = (\lambda^2 - r^2)/(\lambda^2 + r^2)$, where $f(r,\lambda) = 2\lambda r/(r^2 + \lambda^2)$, λ is the skyrmion radius, and β is the chirality angle. For the Néel-type skyrmion, occurring in the considered system, $\beta = 0$ at equilibrium. The total energy E of the system is an integral of the macroscopic energy density W,

$$
E = \int_0^\lambda \int_0^{2\pi} W\,r\,dr\,d\phi.
\tag{7}
$$

Using a set of Euler-Lagrange equations for $\mathcal{L}(\lambda, \beta, \dot{\beta})$, one can derive dynamic equations for $\lambda(t)$ and $\beta(t)$,

$$
\frac{\partial \lambda}{\partial t} = C_1 D(t)\sin\beta,
\tag{8}
$$

$$
\frac{\partial \beta}{\partial t} + G\beta = \frac{C_1 D(t)\cos\beta}{\lambda} + \frac{C_2}{\lambda^4} + C_3\epsilon_{zz}(t) + C_4.
\tag{9}
$$

The given parameters are $D(t) = D_0 + \eta_{iz}\epsilon_{zz}(t)$, artificial damping G, $C_1 = -\gamma/M_s(1 + \ln 4)$, $C_2 = -C_1 a_0^2 A$, $C_3 = 4B_1 C_1(\ln 8 - 2)/3$, and $C_4 = -C_1[K_s(36 - 48\ln 2)/t_f + K_1(48\ln 2 - 31) + 4H_z M_s\mu_0(\ln 64 - 3)]/12$ with magnetoelastic constant B_1, exchange constant A, surface anisotropy, and magnetocrystalline constants K_s and K_1, and Zeeman term $H_z M_s\mu_0$.

Equations (8) and (9) describe the dynamics of the skyrmion's BM driven by elastic longitudinal deformations in the z direction, typically generated by a piezoelectric substrate. In practice, we can introduce in-plane strains ϵ_{xx} and ϵ_{yy} into these equations as static perturbations. However, ϵ_{zz} is considered as a plane wave, which is possible only in the absence of local free surfaces, which means $\epsilon_{xx} = \epsilon_{yy} = 0$.
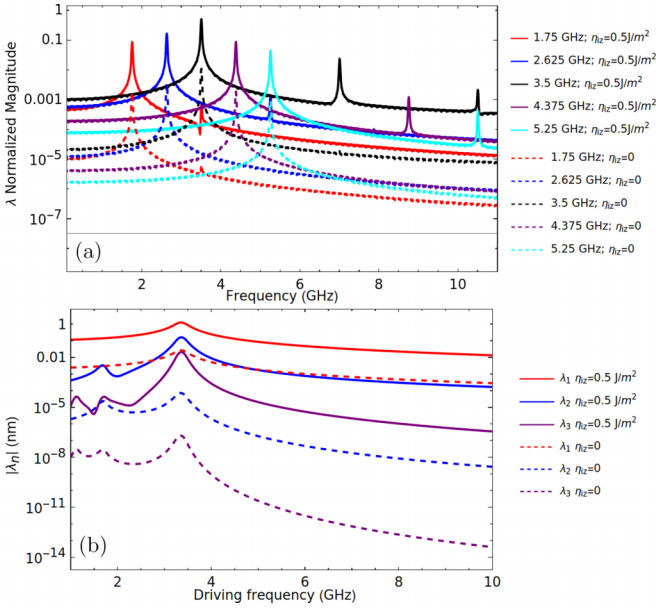
FIG. 2. (a) BM spectra [Fourier transform of $\lambda(t)$] as a function of the driving frequency of an elastic wave with $\eta_{iz} = 0.5$ J/m^2 and $\eta_{iz} = 0$, and (b) response magnitudes λ_1, λ_2, and λ_3 with/without SIDMI as functions of frequency obtained via the HBM.

Equations (8) and (9) can be solved numerically by finite-difference time-domain methodology, in which all differential operators are discretized by the second-order differences, and the solution at a set of time steps is found my marching on in time.

All the following results were obtained using the following material parameters, which are based on experimental data: $\eta_{iz} = 0.5$ J/m^2, $\eta_{ii} = 0.35$ J/m^2, $H_z = 10^5$ A/m, $K_1 = -1560.6$ J/m^3 [24], $K_2 = 0$, $M_s = 16\times10^5$ A/m [25], $\alpha = 0.01$, $A = 2.5\times10^{-11}$ J/m [25], $D_0 = 2.26\times10^{-3}$ J/m^2 [25], $K_s = 1.18\times10^{-3}$ J/m^2 [25], $B_1 = -20.18\times10^6$ J/m^3 [24], $B_2 = -15.27\times10^6$ J/m^3 [24], $c_{11}^{\mathrm{CoFe}} = 259\times10^9$ Pa, $c_{12}^{\mathrm{CoFe}} = 154\times10^9$ Pa, $c_{44}^{\mathrm{CoFe}} = 131\times10^9$ Pa, $\rho^{\mathrm{CoFe}} = 8290$ kg/m^3, $c_{11}^{\mathrm{Mg}} = 259\times10^9$ Pa [26], $c_{12}^{\mathrm{MgO}} = 95.4\times10^9$ Pa [26], $c_{44}^{\mathrm{MgO}} = 153\times10^9$ Pa [26], $\rho^{\mathrm{MgO}} = 3470$ kg/m^3 [26], $c_{11}^{\mathrm{Pt}} = 303\times10^9$ Pa, $c_{12}^{\mathrm{Pt}} = 220\times10^9$ Pa, $c_{44}^{\mathrm{Pt}} = 54\times10^9$ Pa, $\rho^{\mathrm{Pt}} = 21\,447$ kg/m^3. Here, c_{11}, c_{12}, and c_{44} are elastic tensor components for cubic symmetry and ρ is a density.

Figure 2(a) shows the skyrmion radius spectra for the case with/without SIDMI. The spectra were obtained via a numerical solution of Eqs. (8) and (9) for $\epsilon_{zz} = \epsilon_0 \sin 2\pi \nu t$. In this scenario, projections of the DMI vector are also time dependent since $D_i = D_0 + \eta_{iz}\epsilon_{zz}$, which generates a change in the natural frequency of the system. It is evident that SIDMI leads to a major increase of the linear and nonlinear excitation of the BM as compared to the case without considering SIDMI. The enhanced excitation includes an increase of the response magnitude and higher harmonic generation.

To interpret this strong linear and nonlinear excitation, we expand Eqs. (8) and (9) around the equilibrium λ_0 and β_0 including terms up to the second order. Being interested in the steady-state periodic solutions, we use the harmonic balance method (HBM), in which we seek the solution in the form

of harmonics, i.e., Fourier series: $\lambda = \lambda_0 + \sum_n \lambda_n e^{i\omega_n t}$, $\beta = \beta_0 + \sum_n \beta_n e^{i\omega_n t}$ for the elastic perturbations $\epsilon_{zz} = \epsilon_0 e^{i\omega_1 t}$, where $\omega_n = n\omega$ and n is the harmonic number. After the substitution of this solution representation into the second-order approximated equations we obtain the system for kth iteration of nth modes,

$$i\omega_n \lambda_n^k - C_1 D_0 \beta_n^k = \epsilon_0 C_1 \eta_{iz} \beta_{n-1}^{k-1}(1 - \delta_{1,n}), \tag{10}$$

$$i\omega_n \beta_n^k + G\beta_n^k + R\lambda_n^k = \epsilon_0 \left(\frac{C_1 \eta_{iz}}{\lambda_0} + C_3\right)\delta_{1,n}$$
$$- \frac{C_1 D_0}{2\lambda_0} \sum_m \beta_{n-m}^{k-1}\beta_m^{k-1}$$
$$+ F \sum_m \lambda_{n-m}^{k-1}\lambda_m^{k-1},$$
$$- \frac{\epsilon_0 C_1 \eta_{iz}}{\lambda_0^2} \lambda_{n-1}^{k-1}(1 - \delta_{1,n}), \tag{11}$$

where $\beta_0 = 0$ for the Néel-type skyrmions and λ_0 can be found from the equilibrium conditions $\dot{\lambda} = 0$ and $\dot{\beta} = 0$, $R = 4C_2/\lambda_0^5 + C_1 D_0/\lambda_0^2$ and $F = 10C_2/\lambda_0^6 + C_1 D_0/\lambda_0^3$, and for the chosen parameters it is $\lambda_0 = 4.86$ nm.

From Eq. (11), we can make two important conclusions. First, the excitation of the $n = 1$ harmonic, i.e., the linear term proportional to $\delta_{1,n}$, is dominated by the SIDMI rather than by the classical ME effect because, typically, $|C_1 \eta_{iz}/C_3\lambda_0| \approx 10^2$. Second, the higher-harmonic terms, i.e., the terms with $n > 1$ proportional to $(1 - \delta_{1,n})$, are dominated by SIDMI because they originate from nonzero η_{iz}. The solution of the HBM agrees with the time-domain solutions of Eqs. (8) and (9), including the results of Fig. 2(a). The HBM allows obtaining the magnitudes of the first and higher harmonics as shown in Fig. 2(b). We find that all the harmonics are excited much stronger when SIDMI is present.

C. Skyrmion dynamics via magnetoelasticity

Equations (8) and (9) account for the inverse magnetostriction effect with the magnetization influenced by deformations. However, it is more realistic to simultaneously solve ME equations, i.e., coupled equations, in which the wave elastic equation is solved together with the damped LLG equation including the demagnetization energy (W_{dm}) [27,28]. Such a three-dimensional (3D) model also allows introducing nonzero $\eta_{xy} = \eta_{yx} = 0.35$ J/m^2. The elastodynamic equation (12) for the velocities $v_i = \partial u_i/\partial t$ and stresses $\sigma_{ij} = c_{ijkl}\epsilon_{kl}$ in anisotropic crystals describes the relationship between the displacement $\boldsymbol{u}$ and external forces, where the strain tensor components are given by $\epsilon_{ij} = (\partial u_i/\partial j + \partial u_j/\partial i)/2$ [29],

$$\rho\frac{\partial v_i}{\partial t} + \beta v_i = \nabla_j(\sigma_{ij} + \sigma_{ij}^{\mathrm{me}}) + f_i,$$
$$\frac{\partial \sigma_{ij}}{\partial t} = c_{ijkl}\frac{1}{2}\left(\frac{\partial v_k}{\partial l} + \frac{\partial v_l}{\partial k}\right), \tag{12}$$

with open boundary conditions $\partial v_i/\partial i = \pm(c_{11}\rho)^{-1/2}\partial \sigma_{ii}/\partial i$ and $\partial v_j/\partial i = \pm(c_{44}\rho)^{-1/2}\partial \sigma_{ij}/\partial i$. Here, $\sigma_{ij}^{\mathrm{me}} = \partial W_{\mathrm{me}}/\partial \epsilon_{ij}$ is the magnetostriction stress tensor, ρ is the density, β is the damping constant, and f_i is the force density. This system of
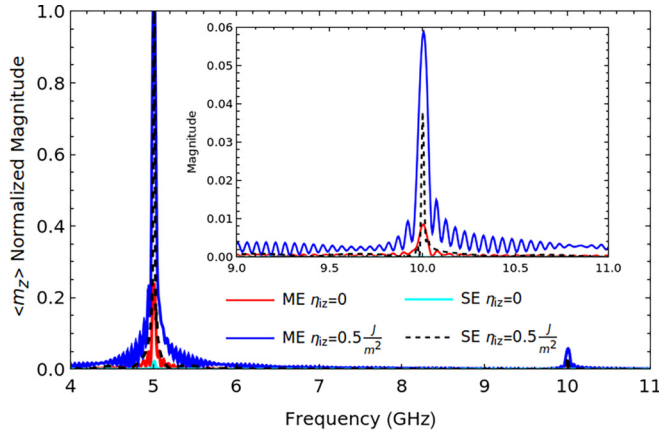
FIG. 3. BM spectra obtained via ME equations and SEs for the elastic wave driving frequency of 5 GHz and amplitude of 0.03% of deformations.

ME first-order differential equations is solved using a leapfrog scheme [30–32].

We start ME simulations by initially distributing a single skyrmion within a 2D CoFe layer. The LLG equation is solved only in the 2D CoFe region, while the elastic equations involve a 3D trilayer system comprising MgO (6.3 nm)/CoFe (0.7 nm)/Pt (6.3 nm) with each layer divided into a grid of cells. Specifically, we use a grid size of $64 \times 64 \times 19$ cells in the x, y, and z dimensions, respectively, with the cell sizes $d_x = d_y = 1.5$ nm, $d_z = 0.7$ nm. The cell characteristic size is less than the exchange length because $\lambda \sim l_{ex}$. The skyrmion creates its deformation field (Fig. 3). We simulate the transducer influence via introducing a force density $f_z = \epsilon_0 c_{11} \sin(2\pi \nu t)/d_z$ at the bottom layer of MgO. This allows keeping this boundary open, which is equivalent to the case, in which elastic waves propagate into the trilayer from the substrate.

As the skyrmion forms within the CoFe layer it induces strain fields due to the magnetostriction effect, resulting in deformations at a scale of approximately $10^{-3}\%$.

Figure 3 compares the BM spectra, i.e., the dependence of the Fourier transform of the $\langle m_z \rangle$ versus the frequency, obtained via two approaches: SE and ME for the $\epsilon_0 = 0.0003$ with $\nu = 5$ GHz. It is evident that ME and SE results show a greatly enhanced first- and higher-harmonic excitations. ME also shows a stronger nonlinear excitation even in the case of $\eta_{iz} = 0$.

Figure 4 shows the ratio of the second- and first-harmonic magnitudes as a function of the driving excitation amplitude and frequency. For the half of the resonance frequency of 1.75 GHz, this ratio is maximal and reaches 80% at the amplitude of the phonon wave ϵ_{zz} of only 0.02%, which is around 420% enhancement. For frequencies greater than 10 GHz, the second-harmonic magnitude is about 3%−5% of the excitation, which is still around 30 times stronger than
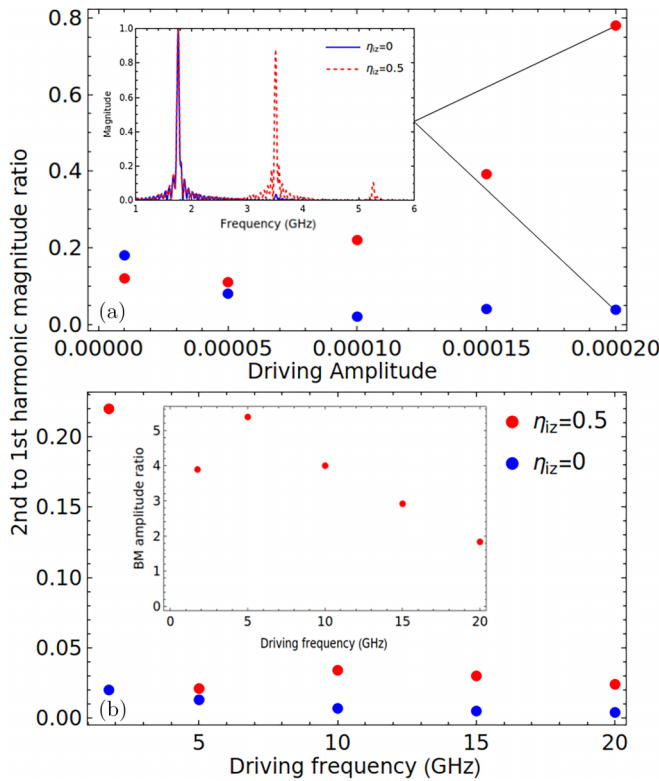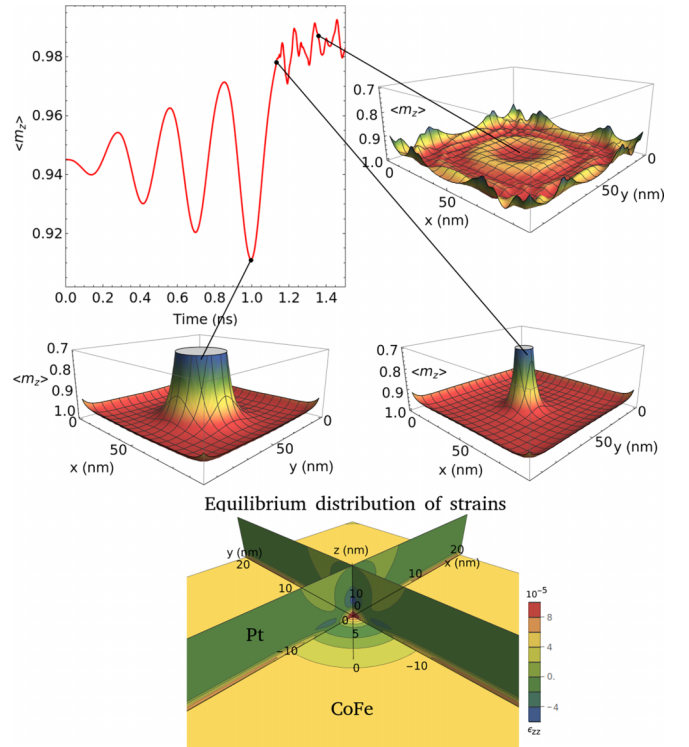

FIG. 4. The ratios between the magnitudes of the $n = 2$ to $n = 1$ harmonics as a function of the elastic wave amplitude of (a) 1.75 GHz and (b) 0.01% of deformations. The inset in (b) shows the ratio of the real-space BM amplitudes for $\eta_{iz} = 0.5$ (with SIDMI) and $\eta_{iz} = 0$ (without SIDMI).

FIG. 5. Collapse of the skyrmion induced by 0.01% of ϵ_{zz} strains at resonance frequency 3.6 GHz with $\eta_{iz} = 0.5$ J/m^2, $\eta_{xy} = 0.35$ J/m^2. The top left figure shows the evolution of $\langle m_z \rangle$ starting from the equilibrium state. The 3D plots illustrate spatial distributions of m_z at 0.91, 1.01, and 1.12 ns. The bottom slice plot illustrates equilibrium ϵ_{zz} distribution obtained due to ME coupling.

in the case of no SIDMI with only 0.1% second-harmonic magnitude.

The skyrmion BM response driven by SIDMI can become so strong that the skyrmion can be completely destroyed. Figure 5 demonstrates the collapse of the skyrmion induced by only 0.01% of ϵ_0 at 3.6 GHz. For the fixed amplitude of 0.01%, we find that the skyrmion is destroyed in the range of 3.2–3.9 GHz.

III. SUMMARY

We explored giant phonon-skyrmion coupling due to the interactions between the skyrmion's BM and time-dependent SIDMI. To analyze the BM, we used SEs of motion as well as coupled ME equations. SEs allow for a simplified analysis, which is further elucidated by via the HBM. Such an analysis shows that SIDMI plays a crucial role in the skyrmion's BM dynamics. ME equations demonstrate realistic operation, verifying the fundamental findings of the SEs. The results showed that SIDMI leads to a major enhancement of the skyrmion's BM dynamics. The enhancement includes major increases of the first- and higher-harmonic magnitudes of the BM, which reach the levels of more than 400% as compared

to no SIDMI. The enhanced dynamics can be so strong that it can lead to the skyrmion collapse, so that skyrmions can be deleted with a weak strain-induced excitation. This giant SIDMI effects open possibilities for an efficient manipulation of skyrmions, and, more generally, efficient manipulation of nanomagnetic structures by strain, offering opportunities for electronics applications.

[1] N. D'Souza, A. Biswas, H. Ahmad, M. S. Fashami, M. M. Al-Rashid, V. Sampath, D. Bhattacharya, M. A. Abeed, J. Atulasimha, and S. Bandyopadhyay, Energy-efficient switching of nanomagnets for computing: straintronics and other methodologies, Nanotechnology **29**, 442001 (2018).

[2] K. Roy, S. Bandyopadhyay, and J. Atulasimha, Hybrid spintronics and straintronics: A magnetic technology for ultra low energy computing and signal processing, Appl. Phys. Lett. **99**, 063108 (2011).

[3] E. Savostin and N. Pertsev, Superconducting straintronics via the proximity effect in superconductor–ferromagnet nanostructures, Nanoscale **12**, 648 (2020).

[4] D. Crum, M. Bouhassoune, and J. Bouaziz, Perpendicular reading of single confined magnetic skyrmions, Nat. Commun. **6**, 8541 (2015).

[5] A. Chumak, V. Vasyuchka, B. Serga, and B. Hillebrands, Magnon spintronics, Nat. Phys. **11**, 453 (2015).

[6] G. Bourianoff, D. Pinna, M. Sitte, and K. Everschor-Sitte, Potential implementation of reservoir computing models based on magnetic skyrmions, AIP Adv. **8**, 055602 (2018).

[7] H. Yang, A. Thiaville, S. Rohart, A. Fert, and M. Chshiev, Erratum: Anatomy of Dzyaloshinskii-Moriya interaction at Co/Fe interfaces, Phys. Rev. Lett. **118**, 219901(E) (2017).

[8] A. Soumyanarayanan, N. Reyren, A. Fert, and C. Panagopoulos, Emergent phenomena induced by spin-orbit coupling at surfaces and interfaces, Nature (London) **539**, 509 (2016).

[9] Y. Iguchi, S. Uemura, K. Ueno, and Y. Onose, Nonreciprocal magnon propagation in a noncentrosymmetric ferromagnet, Phys. Rev. B **92**, 184419 (2015).

[10] S. Seki, Y. Okamura, K. Kondou, K. Shibata, M. Kubota, R. Takagi, F. Kagawa, M. Kawasaki, G. Tatara, Y. Otani, and Y. Tokura, Magnetochiral nonreciprocity of volume spin wave propagation in chiral-lattice ferromagnets, Phys. Rev. B **93**, 235131 (2016).

[11] J.-M. Hu, T. Yang, and L.-Q. Chen, Stability and dynamics of skyrmions in ultrathin magnetic nanodisks under strain, Acta Mater. **183**, 145 (2020).

[12] D. A. Garanin, R. Jaafar, and E. M. Chudnovsky, Breathing mode of a skyrmion on a lattice, Phys. Rev. B **101**, 014418 (2020).

[13] S. Seki, Y. Okamura, K. Shibata, R. Takagi, N. D. Khanh, F. Kagawa, T. Arima, and Y. Tokura, Stabilization of magnetic skyrmions by uniaxial tensile strain, Phys. Rev. B **96**, 220404(R) (2017).

[14] Z. Li, Y. Zhang, Y. Huang, C. Wang, X. Zhang, Y. Liu, Y. Zhou, W. Kang, S. C. Koli, and N. Lei, Strain-controlled skyrmion creation and propagation in ferroelectric/ferromagnetic hybrid wires, J. Magn. Magn. Mater. **455**, 19 (2018).

[15] R. Yanes, F. Garcia-Sanchez, R. F. Luis, E. Martinez, V. Raposo, L. Torres, and L. Lopez-Diaz, Skyrmion motion induced by voltage-controlled in-plane strain gradients, Appl. Phys. Lett. **115**, 132401 (2019).

[16] J. Hu, T. Yang, and L. Chen, Strain-mediated voltage-controlled switching of magnetic skyrmions in nanostructures, npj Comput. Mater. **4**, 62 (2018).

[17] M. Mochizuki and S. Seki, Magnetoelectric resonances and predicted microwave diode effect of the skyrmion crystal in a multiferroic chiral-lattice magnet, Phys. Rev. B **87**, 134403 (2013).

[18] N. S. Gusev, A. V. Sadovnikov, S. A. Nikitov, M. V. Sapozhnikov, and O. G. Udalov, Manipulation of the Dzyaloshinskii-Moriya interaction in Co/Pt multilayers with strain, Phys. Rev. Lett. **124**, 157202 (2020).

[19] O. G. Udalov and I. S. Beloborodov, Strain-dependent Dzyaloshinskii-Moriya interaction in a ferromagnet/heavy-metal bilayer, Phys. Rev. B **102**, 134422 (2020).

[20] J. Lou, M. Liu, D. Reed, Y. Ren, and N. X. Sun, Giant electric field tuning of magnetism in novel multiferroic FeGaB/lead zinc

niobate-lead titanate (PZN-PT) heterostructures, Adv. Mater. **21**, 4711 (2009).

[21] A. Fert and P. M. Levy, Role of anisotropic exchange interactions in determining the properties of spin-glasses, Phys. Rev. Lett. **44**, 1538 (1980).

[22] A. N. Bogdanov and U. K. Rößler, Chiral symmetry breaking in magnetic thin films and multilayers, Phys. Rev. Lett. **87**, 037203 (2001).

[23] C. Kittel, Physical theory of ferromagnetic domains, Rev. Mod. Phys. **21**, 541 (1949).

[24] R. C. Hall, Magnetic anisotropy and magnetostriction of ordered and disordered cobalt-iron alloys, J. Appl. Phys. **31**, 157S (1960).

[25] M. Belmeguenai, M. S. Gabor, Y. Roussigné, A. Stashkevich, S. M. Chérif, F. Zighem, and C. Tiusan, Brillouin light scattering investigation of the thickness dependence of Dzyaloshinskii-Moriya interaction in CoFe ultrathin films, Phys. Rev. B **93**, 174407 (2016).

[26] K. Marklund and S. A. Mahmoud, Elastic constants of magnesium oxide, Phys. Scr. **3**, 75 (1971).

[27] A. J. Newell, W. Williams, and D. J. Dunlop, A generalization of the demagnetizing tensor for nonuniform magnetization, J. Geophys. Res.: Solid Earth **98**, 9551 (1993).

[28] J. E. Miltat and M. J. Donahue, Numerical micromagnetics: Finite difference methods, in *Handbook of Magnetism and Advanced Magnetic Materials*, edited by H. Kronmüller, S. Parkin, J. E. Miltat, and M. R. Scheinfein (John Wiley & Sons, Hoboken, NJ, 2007), Vol. 2, pp. 742–764.

[29] L. D. Landau, E. M. Lifshitz, L. P. Pitaevskii, and A. M. Kosevich, *Theory of Elasticity*, Course of Theoretical Physics (Butterworth-Heinemann, Oxford, UK, 1986), Vol. 7.

[30] C. T. Schroder, W. R. Scott, and G. D. Larson, Elastic waves interacting with buried land mines: a study using the FDTD method, IEEE Trans. Geosci. Remote Sens. **40**, 1405 (2002).

[31] U. Iturrarán-Viveros and M. Molero-Armenta, GPU computing with OpenCL to model 2D elastic wave propagation: exploring memory usage, Comput. Sci. Discov. **8**, 014006 (2015).

[32] D. C. Calvo, K. E. Rudd, M. Zampolli, W. M. Sanders, and L. D. Bibee, Simulation of acoustic scattering from an aluminum cylinder near a rough interface using the elastodynamic finite integration technique, Wave Motion **47**, 616 (2010).

[33] T. J. Boerner, S. Deems, T. R. Furlani, S. L. Knuth, and J. Towns, Access: Advancing innovation: NSF's advanced cyberinfrastructure coordination ecosystem: Services & support, in *Practice and Experience in Advanced Research Computing*, PEARC '23 (ACM Press, New York, NY, 2023), pp. 173–176.